Nanoscale

Accepted Manuscript

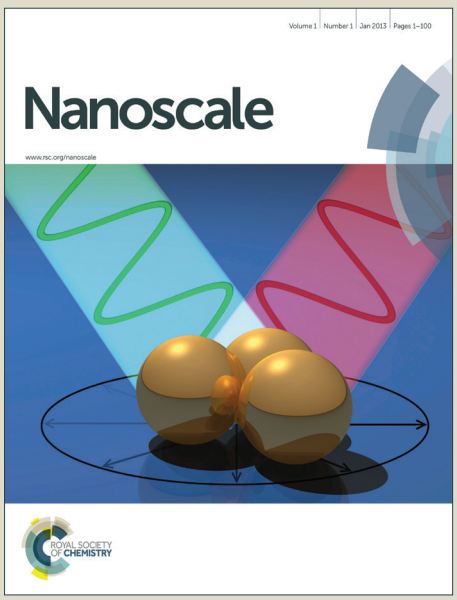

ROYAL SOCIETY OF CHEMISTRY

www.rsc.org/nanoscale

Nanoscale

ARTICLE

Two-step synthesis of luminescent MoS_2-ZnS hybrid quantum dots

Rhiannon M. Clark,[a,b] Benjamin J. Carey,[a,b] Torben Daeneke,*[a] Paul Atkin,[a,b] Madhu Bhaskaran,[c] Kay Latham,[d] Ivan S. Cole[b] and Kourosh Kalantar-zadeh*[a]

Received 00th January 20xx,
Accepted 00th January 20xx

DOI: 10.1039/x0xx00000x

www.rsc.org/

A surfactant assisted technique has been used to promote the exfoliation of molybdenum disulphide (MoS_2) in a water-ethanol mixture, to avoid the use of harsh organic solvents, whilst still producing sufficient concentration of MoS_2 in suspension. The exfoliated flakes are converted into MoS_2 quantum dots (QDs), through a hydrothermal procedure. Alternatively, when the flakes are processed with precursors for zinc sulphide (ZnS) synthesis, a simultaneous break-down and composite growth is achieved. The products are separated by centrifugation, into large ZnS spheres (200-300 nm) and small MoS_2-ZnS hybrid QD materials (<100 nm), of which, the latter show favorable optical properties. Two concurrent photoluminescent (PL) peaks are seen at 380 and 450 nm, which are assigned to MoS_2 and ZnS components of QDs, respectively. The PL emission from MoS_2-ZnS QDs is of high energy and is more intense than the bare MoS_2 flakes or QDs, with a quantum yield as high as 1.96%. The emission wavelength is independent from the excitation wavelength and does not change over time. Due to such properties, the developed hybrid QDs are potentially suitable for imaging and sensing applications.

Introduction

Quantum dots (QDs) have been intensely investigated for their interesting size dependent optical and electronic properties. These properties emerge due to bandgap widening when the dimensions of QDs are reduced below the exciton Bohr radius of the respective material. To date, QDs have been optimised for numerous applications including solar cells, light emitting diodes, sensors and bio-imaging,[1, 2] with several products becoming commercially available. Several previously reported examples of QDs are not safe for commercialisation because they are toxic and unstable in many environments.[2, 3] As such, alternative QD materials are still highly sought after. A suitable material would feature a favorable toxicological profile, stability in air or biological media, a high extinction coefficient and a sufficient photoluminescence (PL) yield. Molybdenum disulphide (MoS_2) has been recently identified as a potential QD material candidate, due to its high stability, low toxicity, abundance and suitable optical properties.[4, 5]

The crystal structure of native 2H-MoS_2 is hexagonal, with molybdenum atoms sandwiched between two layers of sulphur atoms in a trigonal prismatic bonding structure.[6] Covalent bonds link the unit cells in two directions, forming layers that are held together by weak Van der Waals forces. MoS_2 does not feature PL in its 2H bulk form due to an indirect bandgap. Exfoliation of the bulk MoS_2, to thin layers, alters the electronic band structure such that an indirect-to-direct band gap transition occurs.[7] Extensive investigation of the exfoliation process has been conducted, through techniques such as mechanical transfer,[8] Li ion intercalation[9] and solvent assisted processes.[10] Single layer MoS_2 features intense optical absorption, PL and a direct bandgap which is significantly wider than the bandgap of multi-layer MoS_2.[11] Pristine monolayer MoS_2 displays only a modest PL yield of 0.4%,[7] and certainly increasing this yield would improve its suitability for imaging and sensing applications.

Confinement of the lateral dimensions of MoS_2 has been shown to lead to further changes of the optical properties.[12, 13] In particles where the radius is comparable to the exciton Bohr radius, the band structure is tuned by quantum confinement. The dual effects of minimised thickness and reduced lateral size further alter the electronic band energy of the material, resulting in shorter wavelength emission. Wilcoxon *et al.*[13] found that the lateral dimensions of MoS_2 have a relatively stronger effect on its optical properties than the thickness does. The lateral dimensions of the particles control the spin-orbit splitting of the valance band causing a blue shift of absorbance and emission peaks.[13]

Recently, several methods have been developed to prepare MoS_2 QDs that produce blue shifted PL. These methods make use of either electrochemical etching,[14, 15] ultra-centrifugation[12] or pre-defined starting dimensions (nanoparticles)[16] to isolate small sized QDs. Very recently a solvothermal method was presented[17] using organic solvents,

[a] School of Electrical and Computer Engineering, RMIT University, Melbourne, Victoria, 3001, Australia
[b] Manufacturing Flagship, CSIRO, Clayton, Victoria, 3169, Australia
[c] Functional Materials and Microsystems Research Group, RMIT University, Melbourne, Victoria, 3000, Australia
[d] School of Applied Science, RMIT University, Melbourne, Victoria, 3001, Australia
* Torben.daeneke@rmit.edu.au, Kourosh.kalantar@rmit.edu.au

Electronic Supplementary Information (ESI) available: Additional XPS graphs, AFM image, PL spectra, SEM image, TEM images, EDX data, XRD patterns and quantum yield calculations included. See DOI: 10.1039/x0xx00000x

but was unsuccessful in aqueous solution. We develop a new two-step method for the synthesis of MoS_2 QDs in aqueous solution, using the surfactant chenodeoxycholic acid (CDCA) to assist in the exfoliation step. This biocompatible molecule was selected because it is a naturally occurring bile acid and has a very similar structure to other cholate molecules used by Smith *et al.*[18] for the successful exfoliation of layered materials. The preparation of a high yield of QDs from bulk powder, without the implementation of any hazardous additives or solvents, as presented herein, has not been previously achieved.

There has been a recent interest in the synthesis of composites using layered materials,[19, 20] including nanoparticle growth on the surface of MoS_2.[21-24] These hybrid structures often show enhanced properties compared to their individual components, making them useful in a range of applications such as photodetectors and catalysts. To our knowledge, no previous examples of hybrid QDs based on MoS_2 have been demonstrated.

One of the problems of MoS_2 QDs, synthesised using liquid based processes, is that the procedure may introduce defects and also generally form metallic edges.[25] These issues reduce the quality of MoS_2 QDs in terms of possible PL yield. A typical strategy to reduce such effects is passivation using a wider bandgap material, which minimally interferes with the light absorption. Surface passivation protects the core and prevents non-radiative recombination occurring in surface trap sites, resulting in enhanced emission from the core.[26] Amongst the passivation materials, zinc sulphide (ZnS) is a popular candidate as its shelling properties have been successfully demonstrated against other QDs.[1] Advantageously, ZnS is a stable, semiconducting sulphide that can exist in either of two crystal structures (i.e. sphalerite or wurtzite). The wurtzite crystal structure is hexagonal, with lattice parameters close to those of MoS_2 encouraging in-registry growth. Considering that ZnS is also a sulphur based compound, its synthesis procedures have good synergy with MoS_2 synthesis processes. Therefore ZnS can potentially be a suitable passivation candidate for use with MoS_2 QDs.

Herein we describe a novel and scalable synthetic method for thin MoS_2-ZnS hybrid QDs. A modified surfactant assisted exfoliation technique has been developed, using the naturally occurring bile acid CDCA. This leads to high exfoliation yields in ethanol water mixtures, while maintaining a green synthesis profile and biocompatibility. We propose a novel hydrothermal method, in which aqueous suspensions of exfoliated laterally large MoS_2 sheets are broken down into QDs. This approach limits one dimension of the QDs through the pre-defined thickness of the precursor flakes. Advantageously, ZnS growth can be achieved simultaneously in the hydrothermal step. The synthesised hybrid MoS_2-ZnS QDs are found to feature superior PL yields with emissions independent from the excitation wavelength, which is sign of a relatively narrow size distribution. The hybrid QDs with stable emission properties are likely to be useful as imaging agents and could be tuned as nanosensors with measurable optical emission.

Experimental

Exfoliation

A modified surfactant assisted method was used for the exfoliation of MoS_2. 1 g of MoS_2 powder (<1 µm size, 99.9% US Nano) was ground in a mortar and pestle with 1.5 mL of acetonitrile for 15 minutes, before adding an additional 1.5 mL and grinding for a further 15 minutes. The ground powder was left to dry for approximately 10 minutes. Meanwhile, 7 mg of chenodeoxycholic acid (CDCA) was dissolved in 40 mL of a 50:50 v/v mixture of ethanol and water, the pH was adjusted to 10 using 30% ammonia. The ground MoS_2 powder was then suspended in 30 mL of the CDCA solution and probe sonicated (QSonica, 500 W, amplitude 20%) for 90 minutes with a pulse ratio of 50:10 seconds. The resulting mixture was centrifuged at 4000 RPM for 90 minutes, to remove sediment powder and obtain the yellow-green MoS_2 suspension (Figure 1 step 1).

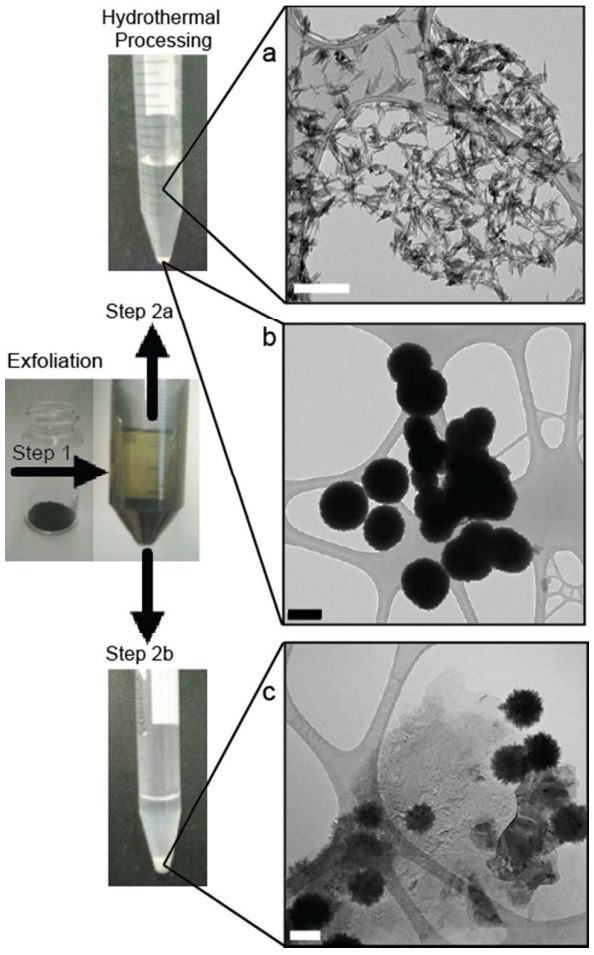

Figure 1. Flow chart of synthetic procedure, with photos at each step, and transition electron microscope (TEM) images of products: (a) Hydrothermal reaction supernatant. (b) Hydrothermal reaction precipitates. (c) Hydrothermal reaction precipitates using sediment MoS_2, scale bars 200 nm.

Hydrothermal processing

For the 0 mM sample, 2 mL of MoS_2 suspension and 8 mL of MilliQ water were mixed and the pH was adjusted to 10 using 30% ammonia. The mixture was stirred for 30 minutes before

transferring to a 50 mL Teflon-lined stainless steel autoclave and kept at 140˚C for 3 hours. The autoclave was cooled to room temperature before transferring the products into a 15 mL tube and centrifuging at 4000 RPM for 60 minutes.
For the time length study, 0 mM solutions (as described above) were heated and removed from the oven at varying times over the course of 24 hours.
For the surfactant control study, samples were prepared using 2 mL of surfactant solution in place of the suspension of MoS_2.

Hydrothermal processing with simultaneous ZnS growth

A 10 mL sample was prepared using 2 mL of the exfoliated MoS_2 suspension, 1 mM zinc nitrate hexahydrate and 2 mM L-cysteine in MilliQ water, the pH was adjusted to 10 using 30% ammonia. The rest of the procedure was similar to the preparation of the 0 mM sample (Figure 1 step 2a). The colourless supernatant was decanted and the white precipitate was re-suspended in MilliQ water. This procedure was repeated over a concentration range of 0.01 to 10 mM zinc nitrate hexahydrate with L-cysteine in a molar ratio of 1:2. The samples are referred to by their zinc content, for instance the sample with 0.4 mM zinc nitrate hexahydrate is called "0.4 mM sample". PL emission zinc sensitivity testing was performed by preparing samples from suspended MoS_2 processed with neither zinc nor cysteine, with only 2 mM cysteine, and with only 1 mM zinc nitrate hexahydrate. PL spectra were collected, then 1 mM zinc nitrate hexahydrate was added to the samples that contained no zinc and PL was again collected. The hydrothermal processing was also repeated using sediment MoS_2 in place of suspended MoS_2 flakes (Figure 1 step 2b).

Characterisation

Optical characterisation of the products was performed on the suspensions, without further treatment, using 1 cm path length cuvettes. Ultra violet- visible spectroscopy (UV-vis) was collected with a Cary 500 spectrometer and photoluminescence spectroscopy (PL) was collected using a Cary Eclipse fluorescence spectrophotometer. Particle size and quality were assessed by transmission electron microscopy (TEM) using a JEOL1010 instrument (100 keV), and high resolution TEM (HRTEM) was performed using a JEOL2100F (80 keV). Samples were dropped onto holey carbon covered copper mesh TEM grids. Raman spectra (Reinshaw inVia) were collected, from samples drop-cast onto silicon substrates, using a 785 nm laser. The elemental composition was studied by x-ray photoelectron spectroscopy (XPS) of samples drop-cast on silicon substrates and also by energy dispersive x-ray spectroscopy (EDX) within the JEOL2100F TEM. XPS (Thermo Scientific K-alpha) was performed using an Al Kα source (λ= 8.3386Å), with an etch step depth calculated to be approximately 2 nm. EDX was collected with an X-max^N 80T detector (Oxford instruments) attached to the JEOL2100F instrument. Crystal structure information was collected on a Bruker D4 Endeavour x-ray diffractometer (XRD) using Cu Kα radiation (λ= 1.5406 Å). Samples were prepared by repeated application and subsequent drying of each suspension onto a glass substrate, until sufficient sample coverage was achieved. Flake thickness was determined by atomic force microscopy (AFM) of a diluted sample dried on a silicon substrate, using a Bruker Dimension Icon in ScanAsyst mode. Scanning electron microscopy (SEM) was performed using an FEI Nova NanoSEM operating at 5 keV, to study the morphology of ZnS growth on MoS_2 that had been drop-casted on a silicon substrate.

Results and discussion

Exfoliation

Suspensions prepared by surfactant assisted exfoliation show characteristic optical properties of typical MoS_2 suspensions. The presence of CDCA does not alter the properties of the exfoliated MoS_2, in agreement with previous reports using surfactant and biomolecule assisted exfoliation.[18, 27, 28] The UV-vis spectrum (Figure 2a) shows absorbance peaks at 665 and 605 nm corresponding respectively with the A and B transitions to the split valence band,[7, 9, 29] as well as a broad absorbance with peaks at approximately 445 and 400 nm corresponding to the C and D transitions.[13, 27]
Commonly reported PL emission for monolayer MoS_2 of large lateral dimension is between 620-670 nm.[7, 9, 30, 31] However, for our flakes PL spectroscopy (Figure 2b) gives a broad, weak emission between 350-450 nm, indicating that the exfoliated material is not made of large monolayer sheets. Such high energy peaks have been reported previously[32-34] for small sized MoS_2 flakes, indicating that the lateral dimensions should be less than 150 nm. However, broad emission indicates polydispersity of sheets' lateral dimensions. The blue shifted peak is ascribed to the hot PL from the K point of the Brillouin zone.[34] The presence of PL indicates the existence of many MoS_2 sheets being less than five monolayers thick. The thickness of the exfoliated flakes was determined by AFM imaging (Figure S1). Measurements on 80 separate flakes resulted in thicknesses of 0.7-2.8 nm, with the majority corresponding to thickness of two layers of MoS_2. To assess the dimensions, a series of TEM images (including Figure 2c) were studied, measurements indicate that the sheets span a broad range of sizes from 30 to 500 nm.
Raman spectroscopy (Figure 2d) of the suspension drop-cast onto a silicon substrate shows characteristic peaks at 409.5 and 384.7 cm^{-1}.[35, 36] These correspond to the A_{1g} out-of-plane and E^1_{2g} in-plane vibrations respectively. The shift of the E^1_{2g} peak in the suspension sample, compared to the sediment, indicates that the exfoliated flakes are made up of very few layers of MoS_2.[37] The peak that appears with the center at 391 cm^{-1} is associated with partial oxidation of the flakes that occurs during the surfactant assisted exfoliation process.[38]
XPS characterisation (Figures 2e and S2) of the drop-cast flakes on silicon shows two overlapping doublets in the Mo 3d energy range. These are assigned to Mo^{6+} with $3d_{5/2}$ at 231.4 eV and $3d_{3/2}$ at 234.6 eV and the expected Mo^{4+} peaks with $3d_{5/2}$ at 229.2 eV and $3d_{3/2}$ at 232.6 eV for Mo in MoS_2.[9, 39] The presence of Mo 3d peaks for both oxidation states suggests that the sample is partially oxidised, in agreement with the Raman spectrum.

The crystal structure of the material was studied by Wide-Angle XRD (Figure 2f). Patterns collected from the sediment MoS_2 (settled by centrifugation of the exfoliation mixture), and the drop-cast suspension of exfoliated MoS_2, differ from each other. The sediment powder closely matches the expected pattern for 2H-MoS_2 (ICCD No. [00-037-1492]). Peaks occur at 14.7˚ (002), 39.9˚ (103), 44.5˚ (006), 50.1˚ (105), 58.6˚ (110) and 60.4˚ (008) in good agreement with the reference pattern. This indicates that there has been no change to the crystal structure of the bulk material during the CDCA assisted exfoliation. However, the film made from suspension of exfoliated flakes gives a diffraction profile that does not match the expected MoS_2 pattern. A relatively large shift of the (002) peak was seen to occur from 14.7° to 9.9°. This change is expected to occur during the exfoliation process as a result of possible insertion of CDCA molecules between the layers, effectively increasing the interlayer spacing of the (002) plane from 0.6 nm to approximately 0.9 nm, which has been similarly reported by others.[40] Sharp peaks indicate that the flakes are highly crystalline. The broad feature centered at approximately 28° appears due to the glass substrate, it is not an indication of poor crystallinity of the sample itself.

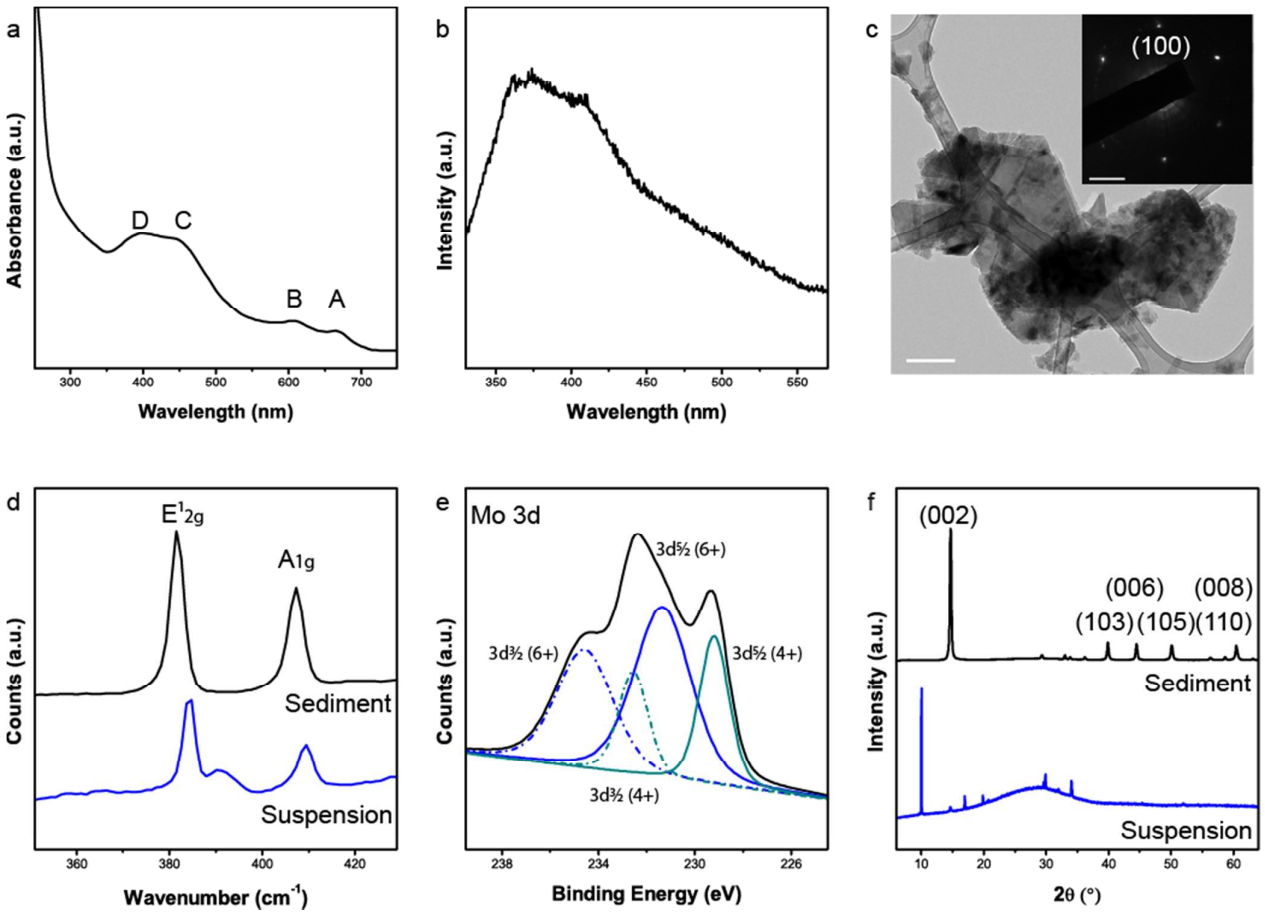

Figure 2. Characterisation of the exfoliated MoS_2 suspension: (a) UV-vis spectrum. (b) PL emission spectrum using 300 nm excitation, (c) TEM image of MoS_2 suspension on holey carbon grid, scale bar 200 nm. Inset SAED pattern of the flake in (c) showing (100) diffraction spots, scale bar 2 nm^{-1}. (d) Raman spectrum, of sediment (black) and suspension (blue) from exfoliation, peaks have been normalised by maximum intensity and offset for ease of comparison. (e) XPS trace of Mo 3d energy range with peaks fitted to the Mo^{6+} and Mo^{4+} oxidation states. (f) XRD patterns of sediment (black) and suspension (blue) from exfoliation, peaks have been normalised by maximum intensity and offset for ease of comparison.

Figure 3a presents a TEM image of a large exfoliated flake. HRTEM (Figure 3b) shows defect free crystal lattice with (100) d spacing of 0.27 nm and (110) d spacing of 0.16 nm,[31] in agreement with the diffraction spots in the selected area electron diffraction (SAED) pattern (Figure 3b inset). This confirms that the crystal structure of the suspended flakes was not significantly altered during the surfactant assisted exfoliation.

Hydrothermal processing

The suspension of exfoliated MoS_2 was processed in a hydrothermal reaction, as described in the Experimental section. The resulting MoS_2 QDs were characterised by HRTEM imaging (Figure 4a). It was observed that most of the particles have close to 5 nm diameter, however large particles are also observed when the well-defined QDs accumulate together.

The MoS_2 QDs have PL emission at 380 nm, with increased intensity relative to the PL from the suspension of exfoliated flakes (before hydrothermal processing). This break-down to small particles with blue-shifted PL is consistent with previous reports on hydrothermal processing of graphene[41] and solvothermal processing of MoS_2.[17] Interestingly, in our case, the emission wavelength is independent from the excitation

wavelength (as discussed below in 'Hydrothermal processing with simultaneous ZnS growth' section), in contrast to several previous reports of excitation dependent emission.[12, 14, 15] This dependence on excitation wavelength is assigned to polydispersity of the sample, with different sized particles causing different emissions. A recent report of highly monodisperse QDs synthesised from MoS_2 nanoparticles[16] also shows excitation wavelength independent emission.

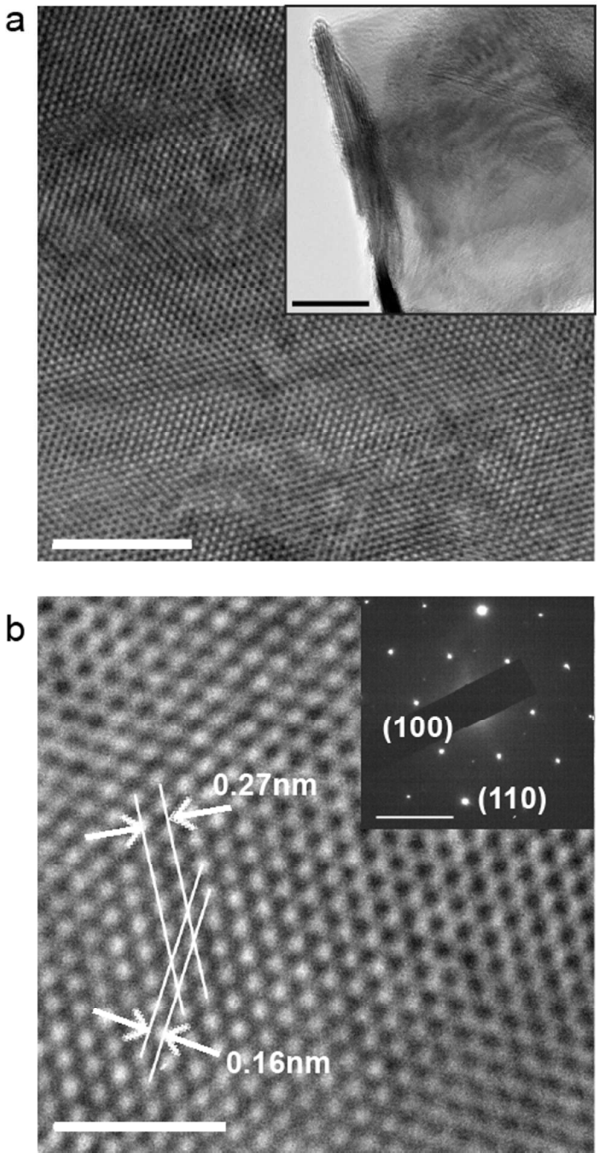

Figure 3. HRTEM of exfoliated MoS_2: (a) MoS_2 flake, scale bar 5 nm. Inset lower magnification, scale bar 20 nm. (b) HRTEM showing MoS_2 lattice with characteristic (100) d spacing of 0.27 nm and (110) d spacing of 0.16 nm, scale bar 2 nm. Inset SAED pattern of exfoliated MoS_2 showing diffraction spots for (100) and (110) planes, scale bar 5 nm^{-1}.

The relationship between the hydrothermal reaction length and PL intensity was studied. It is observed that initially hydrothermal treatment of the MoS_2 flakes slightly reduces the emission intensity, however longer reaction times (>1.5 hours) increase the emission intensity (Figure S3). The intensity is believed to be associated with the number of QD sized particles produced, with longer reaction time causing more complete break-down of the flakes.

Hydrothermal processing with simultaneous ZnS growth

ZnS was grown separately in the presence of sediment or exfoliated MoS_2 *via* a hydrothermal reaction, using zinc nitrate hexahydrate and L-cysteine as described in the Experimental section.

Sediment MoS_2 was first used for studying the nucleation of ZnS onto larger MoS_2 particles. SEM and TEM characterisations (Figures 1c and S4) show large (250 nm diameter) ZnS structures forming from small crystallites (5 nm diameter), some of which nucleated on the MoS_2 surface. The SAED (Figure S4e) shows hexagonally arranged spots diffracted from the MoS_2 crystal and a ring diffracted from polycrystalline ZnS. Dark field images collect from selecting a single spot and part of the ring (Figures S4f and S4g, respectively) give information about the location of each material in the products. It can be seen that ZnS balls have been formed on the surface of the sediment MoS_2, and that each ball is made up of small randomly oriented crystalline ZnS regions.

Hydrothermal synthesis of ZnS in the presence of the exfoliated MoS_2 flakes was performed over a broad zinc concentration range as discussed in the Experimental section. The products were centrifuged at 4000 RPM to separate large precipitates (Figures 1b) from smaller particles that remain in suspension (Figure 1a). The precipitates were characterised by TEM and XPS (Figures 1b and S5) and were determined to be ZnS spheres of 200-300 nm diameter. PL spectroscopy (not shown) did not give any significant emission from the precipitates. XPS analysis confirms that these particles don't contain significant amounts of Mo (Figure S5c) which indicates that most of the Mo should still be present in the supernatant. As such, the supernatants became the focus of further characterisation to determine if MoS_2-ZnS composites had been successfully produced.

TEM images of the hydrothermal reaction supernatants (Figures 1a and S6) show that the ZnS seems to anchor the MoS_2 QDs together to form larger, sub-micron, agglomerates with width 20-30 nm and length <100 nm. The varying zinc concentration doesn't have any major effect on the structure of the particles, however increased amounts of dark regions in the TEM images (Figure S6) indicates thicker particles when the ZnS content is increased. Higher magnification of the 1.0 mM sample, using HRTEM (Figure 4b), shows very small, randomly oriented crystalline regions within the larger structures. Additional HRTEM and dynamic light scattering (Figure S7) reveal individual particles with an average diameter of approximately 6 nm.

In Figure 4c the interference of two overlapping materials can be clearly seen. When fast Fourier transform (FFT) processing is conducted, two separate hexagons are evident (Figure 4d). The diameters of the two rings, 6.1 and 12.5 nm^{-1}, correspond to ZnS (100) and MoS_2 (110), respectively. Applying a mask to each, and performing inverse FFT shows the distribution of each material in the hybrid QD (Figure 4e and f). It is believed that the MoS_2 flakes have been broken to highly monodisperse

QDs as can be seen in Figure 4a and, when the precursors are present, ZnS has simultaneously grown on their surface (Figure 4b). This morphology is consistent with the similar small crystallites which grew on the surface of MoS_2 sediment, joining to form large ZnS balls (Figure S4d).

It is believed that surface defects on the layered MoS_2 provide sites for nucleation of ZnS. The L-cysteine molecules assemble on the MoS_2 surface, and then act as a sulphur source for the growth of ZnS. The synergy of the two hexagonal crystal structures means that ZnS may likely form a layer on top of the MoS_2 basal plane.

The EDX analysis (Figure S8a) gives large peaks for copper from the TEM grid. Closer inspection of the baseline (Figure S8b-d) shows the presence of molybdenum, sulphur and zinc. The presence of ZnS is confirmed by the XRD pattern which is presented in Figure S9.

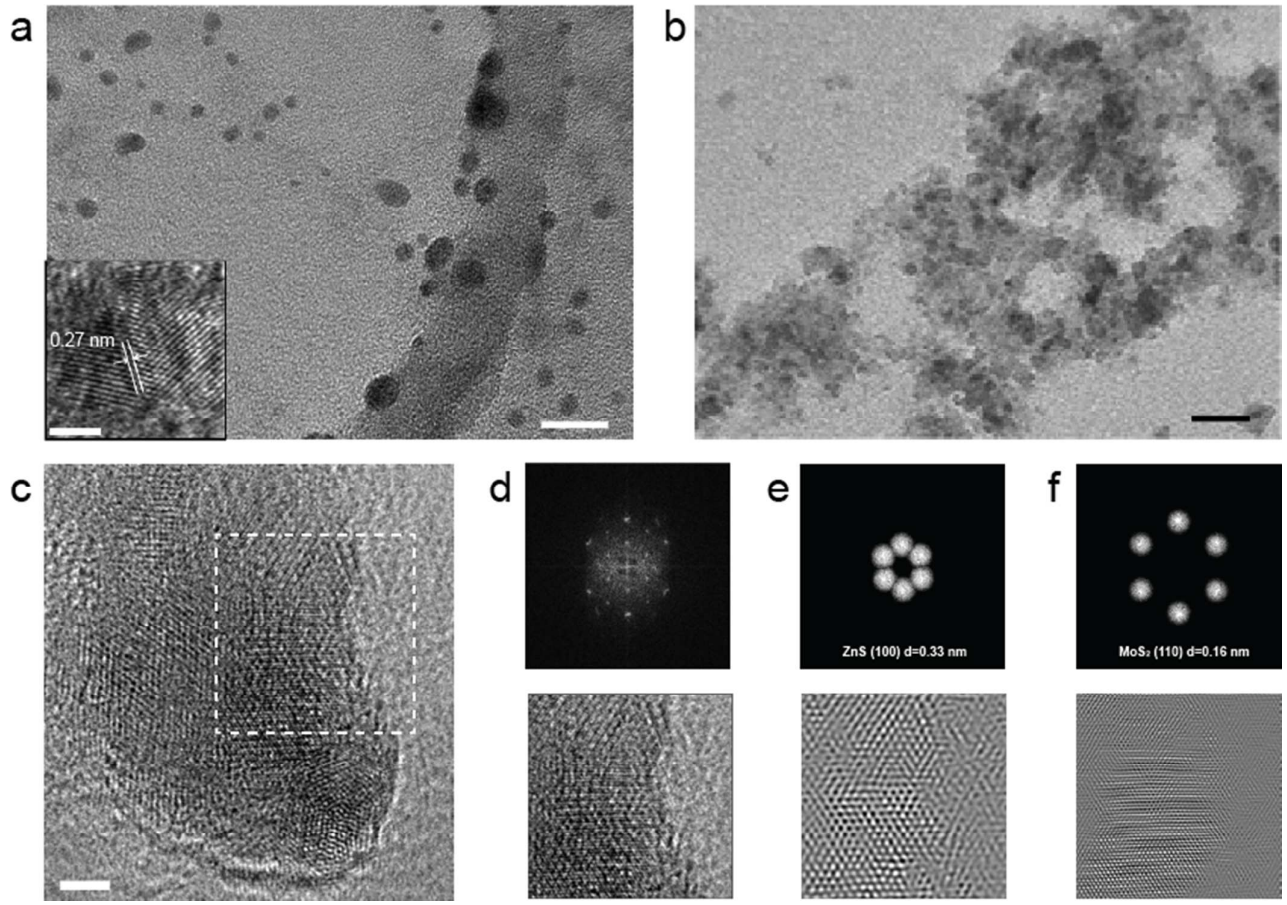

Figure 4. HRTEM of hydrothermal reaction supernatants: (a) 0 mM sample, scale bar 20 nm. Inset higher magnification of two particles, scale bar 2 nm. (b) 1.0 mM sample, scale bar 20 nm. (c) Higher magnification of a hybrid MoS_2-ZnS QD in the 1.0 mM sample, scale bar 2 nm. (d) FFT pattern of selected region from (c). (e) Masked region with diameter of 6.1 nm^{-1} and inverse FFT for ZnS (100). (f) Masked region with diameter of 12.5 nm^{-1} and inverse FFT for MoS_2 (110).

XPS analysis of the supernatants shows molybdenum to be present in two different oxidation states in all of the samples (Figure 5a, d and g). This is due to partial oxidation as previously mentioned. The peak area ratio between the Mo^{6+} state (blue) and Mo^{4+} state (green) indicates the extent of oxidation of each sample. Sulphur appears in two different states in all samples (Figure 5b, e and h), the peak at 169 eV is due to oxidised material and the peak at 162 eV is due to S^{2-} present in MoS_2 and ZnS. The increased relative intensity of the S^{2-} 2p peak (green) indicates that the sample is more reduced when zinc is present.[9, 42] Zinc is absent in the 0 mM sample, and is present as Zn^{2+} in the other samples (Figure 5c, f and i), as expected.

The PL emission from the product supernatants was collected at several excitation wavelengths (Figure S10). The emission from each sample was found to be uniform and independent from the excitation wavelength (Figures 6a and S10).

In contrast to a report by Gan *et al.*,[12] PL collected four weeks after our sample preparation gave the same emission wavelength and intensity as the original measurements (Figure 6a inset), indicating that the samples are very stable.

Except for the 0 mM sample, that only has one peak centered at 380 nm, all hybrid samples are found to have two peaks around 380 and 450 nm, with the peak intensity varying in samples with different zinc concentration (Figure 6b). As the peak at 380 nm (Peak A) is present when there is 0 mM zinc, it is assigned to the MoS_2 emission. As shown in Figure 6c, the intensity of peak A is reasonably unaffected by the zinc concentration from 0.01 to 1 mM with only slight fluctuations, the emission is severely reduced when 5 mM is exceeded. This

indicates that the emission from MoS2 is reduced by the ZnS when in excess, perhaps due to the fact that the majority of photons are absorbed by the ZnS.

The peak at 450 nm (Peak B) is not present for 0 mM zinc, and increases in intensity as the concentration of zinc is increased (Figure 6b). As such, it is expected that peak B is caused by the formation of ZnS onto the MoS_2. PL from ZnS, at wavelengths close to 450 nm, has been recently reported.[43] As shown in Figure 6d, the intensity of peak B changes with zinc concentration and the optimum emission intensity is reliant on the excitation wavelength used. For shorter wavelengths, the most intense emission is seen with 1.0 mM zinc. With longer excitation wavelengths, the maximum emission is achieved with 5.0 mM zinc. These results indicate that MoS_2 excitation is competing at shorter wavelengths, but at longer wavelengths the bandgap energy of MoS_2 is not overcome, only ZnS is excited and hence, more emission is produced.

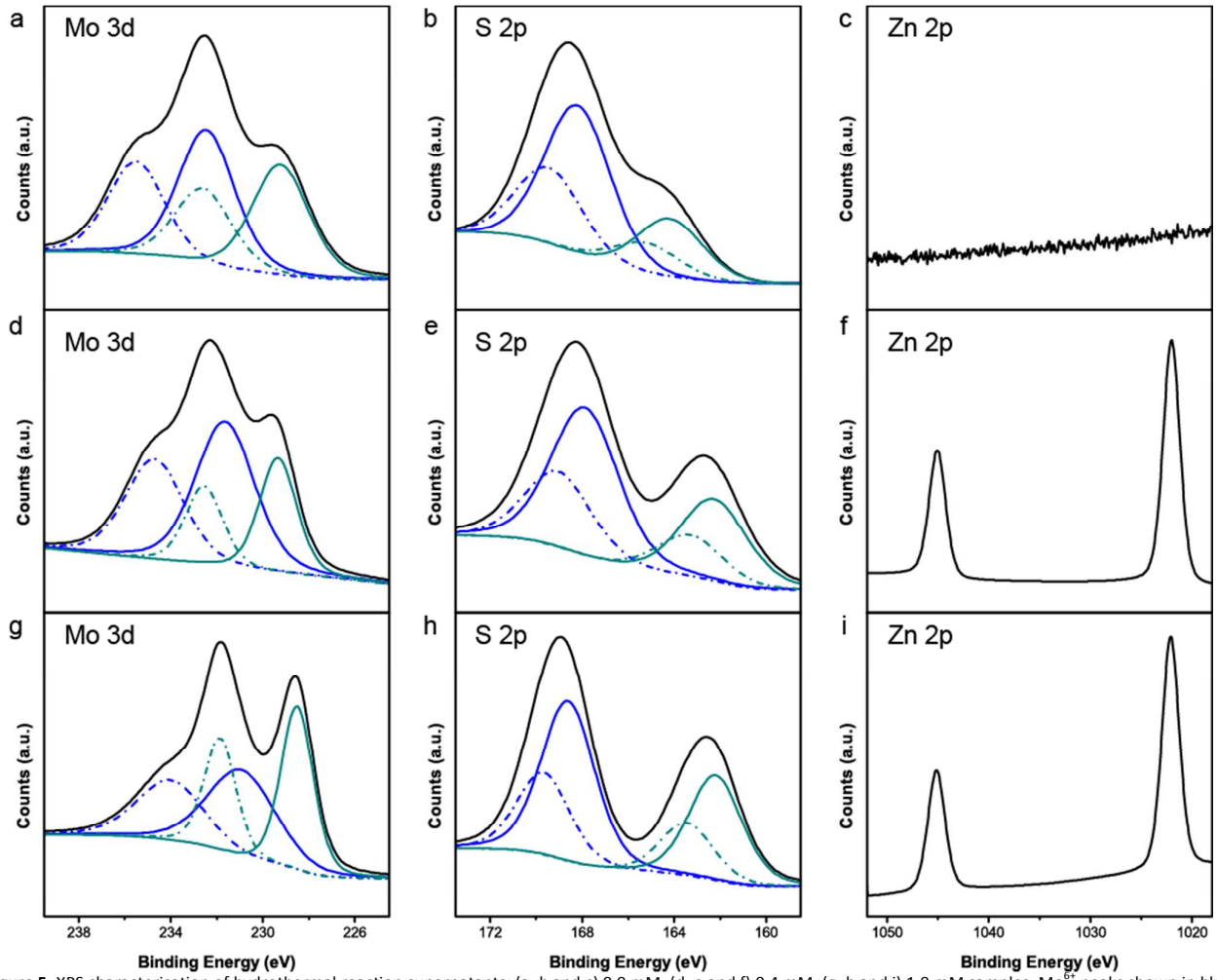

Figure 5. XPS characterisation of hydrothermal reaction supernatants: (a, b and c) 0.0 mM, (d, e and f) 0.4 mM, (g, h and i) 1.0 mM samples. Mo^{6+} peaks shown in blue and Mo^{4+} peaks shown in green, $3d_{5/2}$ solid and $3d_{3/2}$ dashed. S^{2+} peaks shown in blue and S^{2-} peaks shown in green, $2p_{3/2}$ solid and $2p_{1/2}$ dashed.

To confirm that peak B is from the reaction products, and not produced by mixing zinc nitrate hexahydrate with the products, a PL sensitivity test was conducted (as described in the Experimental section). The results (Figure S11) indicate that peak B is only present when MoS_2 is processed with both L-cysteine and zinc nitrate hexahydrate. The peak does not appear when zinc is added to the zinc-free products after the reaction, indicating that the emission at 450 nm is from the product ZnS formed during the hydrothermal reaction.

PL emission from possible by-products of the reaction were ruled out by investigating hydrothermal processing of the surfactant solution without the addition of MoS_2, resulting in no emission (Figure S12). ZnS was also grown in the presence of CDCA surfactant solution containing no MoS_2 and this produced luminescent ZnS with lower quantum yield than from either the bare or hybrid QDs (Figure S12).

The quantum yield of the 0.8 mM sample was calculated (Table S1) to be 1.96%, using quinine sulphate in 0.1 M H_2SO_4 as a reference. This is higher than previously reported (~0.4%) for MoS_2 monolayers[7] and for QDs of MoS_2 synthesised from bulk powder (0.3%)[12] or synthesised from monodisperse nanoparticles (1.3%).[16] The PL quantum yield from the hybrid QDs is much higher than for the bare MoS_2 QDs or the exfoliated flakes, as can be seen in Figure S12. It seems that

the presence of ZnS is enhancing the quantum yield by providing an alternative recombination pathway. Such recombination pathways have also been proposed in a core-shell QD study.[44]

This simple process for synthesising hybrid QDs with strong PL emission provides a pathway to realising a multitude of optical sensors. Through further functionalisation, it is believed that these materials could become sensitive to a large variety of analytes. The introduction of a double peak in the emission spectrum could provide a means for isolation of the two emission wavelengths, with the possibility of introducing sensitivity at one wavelength and using the other wavelength as a reference standard.

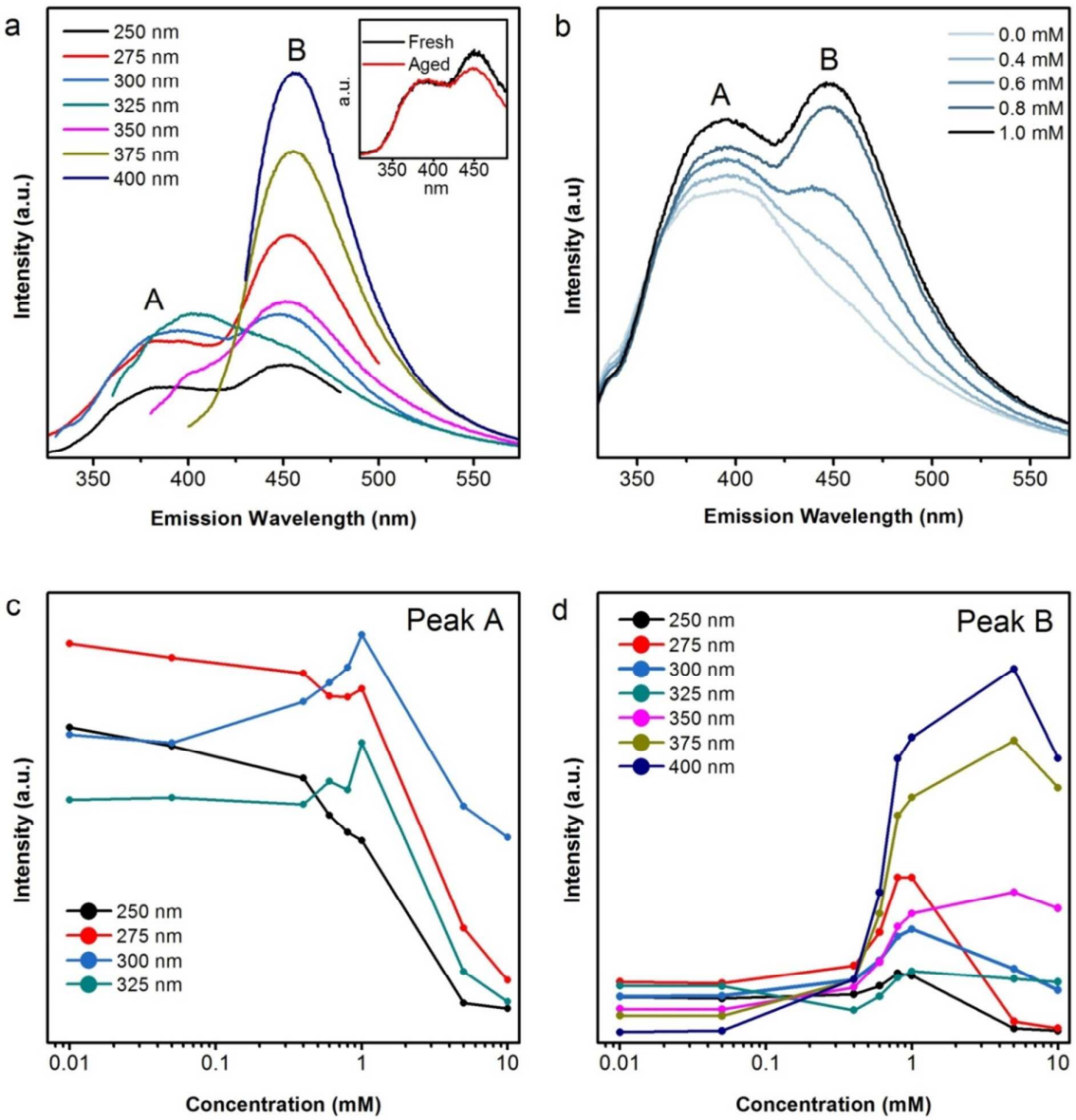

Figure 6. PL emission from hydrothermal reaction supernatants: (a) PL emission from 0.8 mM sample with excitation wavelengths of 250, 275, 300, 325, 350, 375 and 400 nm. Inset PL emission from fresh and aged (4 weeks) 0.8 mM sample using 250 nm excitation. (b) PL emission from 0, 0.4, 0.6, 0.8 and 1.0 mM samples, using 300 nm excitation. PL emission from all samples at other excitation wavelengths is presented in Figure S10. (c) Peak A (380 nm emission) intensity as a function of zinc concentration at excitation wavelengths of 250, 275, 300 and 325 nm. (d) Peak B (450 nm emission) intensity as a function of zinc concentration at excitation wavelengths of 250, 275, 300, 325, 350, 375 and 400 nm.

Conclusions

MoS_2 was exfoliated with a high yield of flakes, in a water and ethanol solution using CDCA surfactant. The hydrothermal processing was shown to break-down the flakes into QDs and result in enhanced optical properties due to quantum confinement. For producing the hybrids, ZnS was formed simultaneously during the hydrothermal process, and has been shown to grow onto large MoS_2 sediment as well as onto MoS_2 QDs. ZnS grew in the form of balls made of small crystallites onto the MoS_2 sediment, but on MoS_2 QDs, ZnS formed thin

layers, that sometimes fused the QDs into sub-micron hybrids. The PL from the hybrid QD products is enhanced (maximum quantum yield of 1.96%) compared to the bare MoS_2 flakes or QDs, indicating that this composite material could be potentially useful for effective optical imaging or sensing applications. We presented the first report on a hydrothermal process for forming MoS_2-ZnS hybrid QDs. Processes may be similarly adopted for forming other metal chalcogenide or oxide compounds onto MoS_2 for obtaining interesting composites with a plethora of functionalities.

Acknowledgements

The authors acknowledge the support of the Commonwealth Scientific and Industrial Research Organisation (CSIRO) and the equipment and technical assistance provided at the RMIT Microscopy and Microanalysis Facility (RMMF) at RMIT University.

Notes and references

1. J. Y. Kim, O. Voznyy, D. Zhitomirsky and E. H. Sargent, *Adv. Mater.*, 2013, **25**, 4986-5010.
2. D. Bera, L. Qian, T. K. Tseng and P. H. Holloway, *Materials*, 2010, **3**, 2260-2345.
3. M. F. Frasco and N. Chaniotakis, *Sensors*, 2009, **9**, 7266-7286.
4. Q. H. Wang, K. Kalantar-Zadeh, A. Kis, J. N. Coleman and M. S. Strano, *Nat. Nanotechnol.*, 2012, **7**, 699-712.
5. W. Z. Teo, E. L. K. Chng, Z. Sofer and M. Pumera, *Chem. - Eur. J.*, 2014, **20**, 9627-9632.
6. M. Chhowalla, H. S. Shin, G. Eda, L. J. Li, K. P. Loh and H. Zhang, *Nat. Chem.*, 2013, **5**, 263-275.
7. K. F. Mak, C. Lee, J. Hone, J. Shan and T. F. Heinz, *Phys. Rev. Lett.*, 2010, **105**, 136805.
8. D. J. Late, B. Liu, H. Matte, C. N. R. Rao and V. P. Dravid, *Adv. Funct. Mater.*, 2012, **22**, 1894-1905.
9. G. Eda, H. Yamaguchi, D. Voiry, T. Fujita, M. Chen and M. Chhowalla, *Nano Lett.*, 2011, **11**, 5111-5116.
10. J. N. Coleman, M. Lotya, A. O'Neill, S. D. Bergin, P. J. King, U. Khan, K. Young, A. Gaucher, S. De, R. J. Smith, I. V. Shvets, S. K. Arora, G. Stanton, H. Y. Kim, K. Lee, G. T. Kim, G. S. Duesberg, T. Hallam, J. J. Boland, J. J. Wang, J. F. Donegan, J. C. Grunlan, G. Moriarty, A. Shmeliov, R. J. Nicholls, J. M. Perkins, E. M. Grieveson, K. Theuwissen, D. W. McComb, P. D. Nellist and V. Nicolosi, *Science*, 2011, **331**, 568-571.
11. A. Kuc, N. Zibouche and T. Heine, *Phys. Rev. B*, 2011, **83**, 245213.
12. Z. X. Gan, L. Z. Liu, H. Y. Wu, Y. L. Hao, Y. Shan, X. L. Wu and P. K. Chu, *Appl. Phys. Lett.*, 2015, **106**, 233113.
13. J. P. Wilcoxon, P. P. Newcomer and G. A. Samara, *J. Appl. Phys.*, 1997, **81**, 7934-7944.
14. B. L. Li, L. X. Chen, H. L. Zou, J. L. Lei, H. Q. Luo and N. B. Li, *Nanoscale*, 2014, **6**, 9831-9838.
15. D. Gopalakrishnan, D. Damien, B. Li, H. Gullappalli, V. K. Pillai, P. M. Ajayan and M. M. Shaijumon, *Chem. Commun.*, 2015, **51**, 6293-6296.
16. H. D. Ha, D. J. Han, J. S. Choi, M. Park and T. S. Seo, *Small*, 2014, **10**, 3858-3862.
17. S. J. Xu, D. Li and P. Y. Wu, *Adv. Funct. Mater.*, 2015, **25**, 1127-1136.
18. R. J. Smith, P. J. King, M. Lotya, C. Wirtz, U. Khan, S. De, A. O'Neill, G. S. Duesberg, J. C. Grunlan, G. Moriarty, J. Chen, J. Z. Wang, A. I. Minett, V. Nicolosi and J. N. Coleman, *Adv. Mater.*, 2011, **23**, 3944-3948.
19. J. L. Gunjakar, I. Y. Kim, J. M. Lee, Y. K. Jo and S.-J. Hwang, *J. Phys. Chem. C*, 2014, **118**, 3847-3863.
20. X. Huang, C. L. Tan, Z. Y. Yin and H. Zhang, *Adv. Mater.*, 2014, **26**, 2185-2204.
21. Z. H. Cheng, B. Z. He and L. Zhou, *J. Mater. Chem. A*, 2015, **3**, 1042-1048.
22. X. Huang, Z. Y. Zeng, S. Y. Bao, M. F. Wang, X. Y. Qi, Z. X. Fan and H. Zhang, *Nat. Commun.*, 2013, **4**, 1444.
23. J. Schornbaum, B. Winter, S. P. Schießl, F. Gannott, G. Katsukis, D. M. Guldi, E. Spiecker and J. Zaumseil, *Adv. Funct. Mater.*, 2014, **24**, 5798-5806.
24. T. S. Sreeprasad, P. Nguyen, N. Kim and V. Berry, *Nano Lett.*, 2013, **13**, 4434-4441.
25. A. Ambrosi, Z. Sofer and M. Pumera, *Chem. Commun.*, 2015, **51**, 8450-8453.
26. P. Reiss, M. Protiere and L. Li, *Small*, 2009, **5**, 154-168.
27. B. L. Li, H. L. Zou, L. Lu, Y. Yang, J. L. Lei, H. Q. Luo and N. B. Li, *Adv. Funct. Mater.*, 2015, **25**, 3541-3550.
28. W. Zhang, Y. Wang, D. Zhang, S. Yu, W. Zhu, J. Wang, F. Zheng, S. Wang and J. Wang, *Nanoscale*, 2015, **7**, 10210-10217.
29. S. Z. Butler, S. M. Hollen, L. Y. Cao, Y. Cui, J. A. Gupta, H. R. Gutierrez, T. F. Heinz, S. S. Hong, J. X. Huang, A. F. Ismach, E. Johnston-Halperin, M. Kuno, V. V. Plashnitsa, R. D. Robinson, R. S. Ruoff, S. Salahuddin, J. Shan, L. Shi, M. G. Spencer, M. Terrones, W. Windl and J. E. Goldberger, *ACS nano*, 2013, **7**, 2898-2926.
30. Q. Q. Ji, Y. F. Zhang, T. Gao, Y. Zhang, D. L. Ma, M. X. Liu, Y. B. Chen, X. F. Qiao, P. H. Tan, M. Kan, J. Feng, Q. Sun and Z. F. Liu, *Nano Lett.*, 2013, **13**, 3870-3877.
31. Y. L. Liu, H. Y. Nan, X. Wu, W. Pan, W. H. Wang, J. Bai, W. W. Zhao, L. T. Sun, X. R. Wang and Z. H. Ni, *ACS nano*, 2013, **7**, 4202-4209.
32. Y. C. Wang, J. Z. Ou, S. Balendhran, A. F. Chrimes, M. Mortazavi, D. D. Yao, M. R. Field, K. Latham, V. Bansal, J. R. Friend, S. Zhuiykov, N. V. Medhekar, M. S. Strano and K. Kalantar-zadeh, *ACS nano*, 2013, **7**, 10083-10093.
33. E. P. Nguyen, B. J. Carey, T. Daeneke, J. Z. Ou, K. Latham, S. Zhuiykov and K. Kalantar-zadeh, *Chem. Mater.*, 2015, **27**, 53-59.
34. J. Z. Ou, A. F. Chrimes, Y. C. Wang, S. Y. Tang, M. S. Strano and K. Kalantar-zadeh, *Nano Lett.*, 2014, **14**, 857-863.
35. R. Ganatra and Q. Zhang, *ACS nano*, 2014, **8**, 4074-4099.
36. H. Li, Q. Zhang, C. C. R. Yap, B. K. Tay, T. H. T. Edwin, A. Olivier and D. Baillargeat, *Adv. Funct. Mater.*, 2012, **22**, 1385-1390.
37. C. Lee, H. Yan, L. E. Brus, T. F. Heinz, J. Hone and S. Ryu, *ACS nano*, 2010, **4**, 2695-2700.
38. R. Murugan, A. Ghule, C. Bhongale and H. Chang, *J. Mater. Chem.*, 2000, **10**, 2157-2162.
39. I. S. Kim, V. K. Sangwan, D. Jariwala, J. D. Wood, S. Park, K. S. Chen, F. Y. Shi, F. Ruiz-Zepeda, A. Ponce, M. Jose-Yacaman, V. P. Dravid, T. J. Marks, M. C. Hersam and L. J. Lauhon, *ACS nano*, 2014, **8**, 10551-10558.

40. S. Jeong, D. Yoo, M. Ahn, P. Miro, T. Heine and J. Cheon, *Nat. Commun.*, 2015, **6**, 5763.
41. D. Y. Pan, J. C. Zhang, Z. Li and M. H. Wu, *Adv. Mater.*, 2010, **22**, 734-738.
42. S. S. Chou, B. Kaehr, J. Kim, B. M. Foley, M. De, P. E. Hopkins, J. Huang, C. J. Brinker and V. P. Dravid, *Angew. Chem. , Int. Ed.*, 2013, **52**, 4160-4164.
43. G. Wang, B. Huang, Z. Li, Z. Lou, Z. Wang, Y. Dai and M.-H. Whangbo, *Sci. Rep.*, 2015, **5**, 8544.
44. D. E. Nam, W. S. Song and H. Yang, *J. Colloid Interface Sci.*, 2011, **361**, 491-496.